

Communication

# Generation, Transmission, and Amplification of OAM Modes in the PbSe-Doped Ring-Core Fiber Carrying 3D Printed Spiral Phase Plate

Yana Shang <sup>1,\*</sup>, Huimei Wei <sup>1</sup>, Hengfei Guo <sup>1</sup>, Na Chen <sup>1</sup>, Zhenyi Chen <sup>1</sup>, Heming Wei <sup>1</sup> , Kemin Wang <sup>2</sup>, Yanhua Dong <sup>1</sup>, Fufei Pang <sup>1</sup> and Tingyun Wang <sup>1</sup>

<sup>1</sup> Key Laboratory of Specialty Fiber Optics and Optical Access Networks, Joint International Research Laboratory of Specialty Fiber Optics and Advanced Communication, Shanghai University, Shanghai 200444, China

<sup>2</sup> Biomedical Science and Technology Research Center, School of Mechatronic Engineering and Automation, Shanghai University, Shanghai 200444, China

\* Correspondence: ynshang@shu.edu.cn

**Abstract:** Vortex beams carrying orbital angular momentum (OAM) have increasingly attracted attention in the field of optical communication. However, transmission is still an issue due to transmission loss, especially in optical fibers. In this work, we proposed, designed, and fabricated micro spiral phase plates (SPPs) directly on an end facet of a piece of PbSe-doped ring-core fiber (RCF) through two-photon polymerization, realizing the integration of OAM beam generation, transmission, and amplification. The prepared RCF comprises a double-clad structure with a core-clad refractive index difference of 2.2% and the fluorescence range is 1150 nm–1700 nm. The intensity distribution of the OAM beam and the spiral interference fringes were obtained, which indicated that the OAM mode ( $|l|=1, 2, 3, 4$ ) was generated and transmitted directly within the fiber. The small-signal amplification of four OAM modes was accomplished at 1550 nm under a pump power of 634 mW. The on-off gain is  $>13.2$  dB for all modes and the differential mode gain (DMG) is  $<1.7$  dB. The SPP-carrying RCF structure demonstrates the integration of generation, transmission, and amplification of higher-order OAM modes in all-fiber systems.

**Keywords:** OAM mode; SPP; PbSe-doped RCF; amplification; 3D printing



**Citation:** Shang, Y.; Wei, H.; Guo, H.; Chen, N.; Chen, Z.; Wei, H.; Wang, K.; Dong, Y.; Pang, F.; Wang, T. Generation, Transmission, and Amplification of OAM Modes in the PbSe-Doped Ring-Core Fiber Carrying 3D Printed Spiral Phase Plate. *Photonics* **2022**, *9*, 823. <https://doi.org/10.3390/photonics9110823>

Received: 28 September 2022

Accepted: 31 October 2022

Published: 2 November 2022

**Publisher's Note:** MDPI stays neutral with regard to jurisdictional claims in published maps and institutional affiliations.



**Copyright:** © 2022 by the authors. Licensee MDPI, Basel, Switzerland. This article is an open access article distributed under the terms and conditions of the Creative Commons Attribution (CC BY) license (<https://creativecommons.org/licenses/by/4.0/>).

## 1. Introduction

The dramatic growth of Internet traffic has placed higher demands on information transmission rates and communication capacities [1,2]. Vortex beams carry a unique orbital angular momentum (OAM) that has attracted a lot of attention in multiple fields [3–6]. The orthogonality between OAM modes with different topological charges is used to realize the mode-division multiplexing, and theoretically, unlimited transmission capacity can be obtained [7,8]. It has been shown that OAM beams can be transmitted in free space over 143 km, but are affected by atmospheric turbulence [9]. Hence, the integration of OAM generation and transmission is still an issue in the field of optical communication.

Compared with other methods, specially designed optical fibers may be employed to achieve stable transmission of the OAM beam [10,11]. It has been demonstrated that the ring-core fiber (RCF) exhibits a “donut” shaped intensity pattern, which is similar to OAM mode distribution, enabling stable transmission of OAM beams while reducing the differential mode gain (DMG) [12]. However, two key issues should be addressed. One is the generation of the OAM beam. The traditional free-space coupling methods lead to low efficiency and low stability [13]. Currently, utilizing a spiral phase plate (SPP) to generate an OAM beam is one of the most efficient methods, which can be fabricated precisely and quickly by the 3D laser direct writing technique [14–17]. The micro-scale SPP is easier to

integrate with micro-optical and microfluidic platforms. The existing 3D-printed SPPs are fabricated on quartz substrates, single-mode fibers, or lenses [18–23]. The second is the transmission of the OAM beam. Due to the transmission loss in fiber, the working length is limited. Therefore, it is necessary to realize the OAM mode amplification. Typically, an erbium-doped fiber is used to achieve high mode gain, low loss, and low DMG [24–26]. However, erbium ions have a small gain bandwidth and a fixed working band that fail to satisfy the communication demands. It was demonstrated that PbSe quantum dots (QDs) are excellent gain media for broadband amplification in amplifiers owing to their spectral coverage in the near-infrared region, tunable absorption-emission spectra, and high quantum yields [27–29]. To our knowledge, few studies have focused on the OAM amplification based on the PbSe QDs with OAM amplifiers.

In this study, we printed micro SPPs directly on an end facet of a piece of a PbSe-doped RCF using two-photon 3D technology, realizing the integration of OAM beam generation, transmission, and amplification. The SPP was aligned with the center of the fiber tip face so that the generated OAM beam could be transmitted directly along the ring-core region. Finally, an OAM amplifier based on the SPP-carrying fiber was developed to examine the mode-gain characteristics and DMG. OAM mode ( $|l|=1, 2, 3, 4$ ) was generated and transmitted directly within the fiber. The on-off gain is  $>13.2$  dB for all modes and the differential mode gain (DMG) is  $<1.7$  dB, demonstrating the proposed method could be a suitable choice for the integration of OAM generation, transmission, and amplification.

## 2. Design and Simulations

Figure 1a depicts a cross-sectional schematic of the designed PbSe-doped RCF, which is composed of a core, ring core, inner cladding, and outer cladding. Their respective refractive indices are denoted by  $n_1$ ,  $n_2$ ,  $n_3$ , and  $n_4$ . The radius corresponds to  $r_1$ ,  $r_2$ ,  $r_3$ , and  $r_4$ , respectively. The core and inner cladding are doped with borides, whereas the ring core, as the transmission layer, is primarily doped with the gain medium PbSe and the refractive index-improving GeO<sub>2</sub> material. The main material of the outer cladding is SiO<sub>2</sub>. The purpose of the double-cladding structure is to increase the refractive index difference between  $n_2$  and  $n_3$ . We fixed the core radius ( $r_1$ ) and ring core ( $r_2$ ) to be equal to 3  $\mu\text{m}$  and 11  $\mu\text{m}$ , respectively. There is a large refractive-index difference between the ring core and the inner cladding of 2.2%. The structure of the SPP printed on the end face of the double-clad PbSe-doped RCF is depicted in Figure 1b. Moreover, the thickness of the SPP varies with the azimuthal angle  $\varphi$ , and the thickness distribution function of the spiral phase sheet  $h(\varphi)$  is given by [23]:

$$h(\varphi) = h_0 + \frac{\lambda l \varphi}{2\pi(n - n_0)}; \varphi \in [0, 2\pi] \quad (1)$$

where  $l$  and  $\lambda$  denote the topological charge and incident wavelength, respectively, and the thickness of the spiral phase sheet at  $\varphi = 0$  is  $h_0$ . Moreover,  $n$  and  $n_0$  represent the refractive indices of the SPP material and the refractive index of the surrounding medium, respectively.

Thus, the thickness of the phase change  $2\pi$  is:

$$\Delta h = h(2\pi) - h(0) = \frac{\lambda l}{n - n_0} \quad (2)$$

The Femtosecond 3D laser direct writing technology can effectively, flexibly, and quickly develop SPPs. The Gaussian beam enters the SPP from the irregular spiral plane, resulting in different phase delays and spiral wavefronts. When leaving the regular plane, it is converted into an OAM beam which carries a phase factor of  $\exp(il\varphi)$ . The OAM beam is then transmitted directly to the output along the ring core region within the fiber, as shown in Figure 1c.

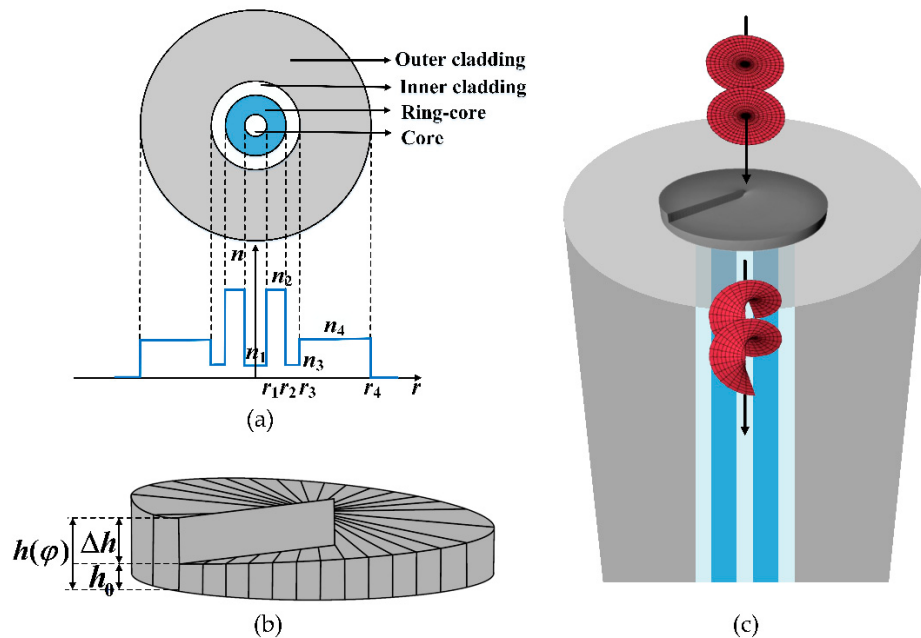


**Figure 1.** (a) Cross-section of the designed PbSe-doped RCF in schematic form; (b) Schematic of the construction of SPP; (c) Schematic of the OAM beam generated by the SPP at the end face of the fiber.

It is well known that based on the finite element method, the vector modes of PbSe-doped RCF can be simulated and calculated by solving differential equations. The parameters were set based on the designed fiber, and the wavelength was 1550 nm. Firstly, a 2D model of the PbSe-doped RCF was constructed and the material properties of each sub-region were added. Then, the boundary conditions were set by adding a perfectly matched layer, while the fiber regions were divided into superfine triangular meshes. Finally, the vector modes of the fiber were obtained by solving the electromagnetic field equations in the module. It was found that the vector modes of the fiber were  $HE_{11}$ ,  $TM_{01}$ ,  $HE_{21}$ ,  $TE_{01}$ ,  $HE_{31}$ ,  $EH_{11}$ ,  $HE_{41}$ ,  $EH_{21}$ ,  $HE_{51}$ ,  $EH_{31}$ ,  $HE_{61}$ ,  $EH_{41}$ ,  $HE_{71}$ , and  $EH_{51}$ . The OAM modes supported by the RCF can be generated by linear superposition of odd and even modes of HE modes and EH modes, which can be defined as [25]:

$$\begin{cases} OAM_{\pm l,m}^{\pm} = HE_{l+1,m}^e \pm iHE_{l+1,m}^o \\ OAM_{\pm l,m}^{\mp} = EH_{l-1,m}^e \pm iEH_{l-1,m}^o \end{cases} \quad (3)$$

where, the upper corner  $\pm$  indicates its polarization direction, which is related to spin angular momentum (SAM), and the lower corner  $\pm l,m$  is related to OAM, where  $\pm$  indicates the direction of phase rotation (+ indicates counterclockwise, - indicates clockwise),  $l$  is the topological charge and  $m$  indicates the radial mode number. Thus, the fiber can support the OAM mode with  $|l|= 1, 2, 3, 4, 5, 6$ .

Because the effective refractive index difference between the vector modes synthesizing the same order OAM mode does not reach  $10^{-4}$ , the vector modes degenerate as linearly polarized (LP) modes. The LP mode may be overlaid to obtain the OAM mode, which can be expressed as follows [30]:

$$\begin{cases} \hat{x}OAM_{\pm l,m} = LP_{l,m}^{c,x} \pm iLP_{l,m}^{s,x} \\ \hat{y}OAM_{\pm l,m} = LP_{l,m}^{c,y} \pm iLP_{l,m}^{s,y} \end{cases} \quad (4)$$

where,  $\hat{x}$  and  $\hat{y}$  represent the x- and y-polarization directions, respectively. The superscripts  $c$  and  $s$  denote the cosine and sine functions corresponding to the even and odd modes of the LP mode, respectively.

OAM mode purity is an important parameter to measure the transmission characteristics of OAM fibers. Higher OAM purity means more stable mode transmission, allowing it to be better employed for OAM multiplexing. The magnitude of the mode purity depends on the intensity of the light superposition factor, as the following expression [31]:

$$\eta = \frac{I_r}{I_c} = \frac{\iint_{\text{ring}} |\vec{E}|^2 dx dy}{\iint_{\text{cross-section}} |\vec{E}|^2 dx dy} \quad (5)$$

where,  $I_r$  and  $I_c$  denote the electric field intensity of the ring region inside the RCF and the 2D cross-section of RCF, respectively. The results of the OAM purity are shown in Table 1. The simulation shows that the purity of the OAM mode that the fiber can support is greater than 98%.

**Table 1.** OAM mode purity ( $|l| = 1 \sim 6$ ).

OAM Mode	$ l =1$	$ l =2$	$ l =3$	$ l =4$	$ l =5$	$ l =6$
purity	99.4%	99.4%	99.3%	99.1%	98.4%	98.4%

This study focuses on the generation, transmission, and amplification of OAM modes for  $|l| = 1, 2, 3, 4$ . The SPP is designed with a diameter of 60  $\mu\text{m}$ , a spiral height ( $\Delta h$ ) of 2.98  $\mu\text{m}$  at 1550 nm, and a substrate height of 3  $\mu\text{m}$ . The normalized mode intensity and phase distribution of the OAM modes generated by the SPP based on simulations of the design data are illustrated in Figure 2. It is known that there is a phase singularity at the center of the vortex beam, resulting in the central light intensity being zero. It can be observed that the beam intensity distribution exhibits a doughnut shape. The region in which the central intensity is zero gradually expands as the OAM order increases.

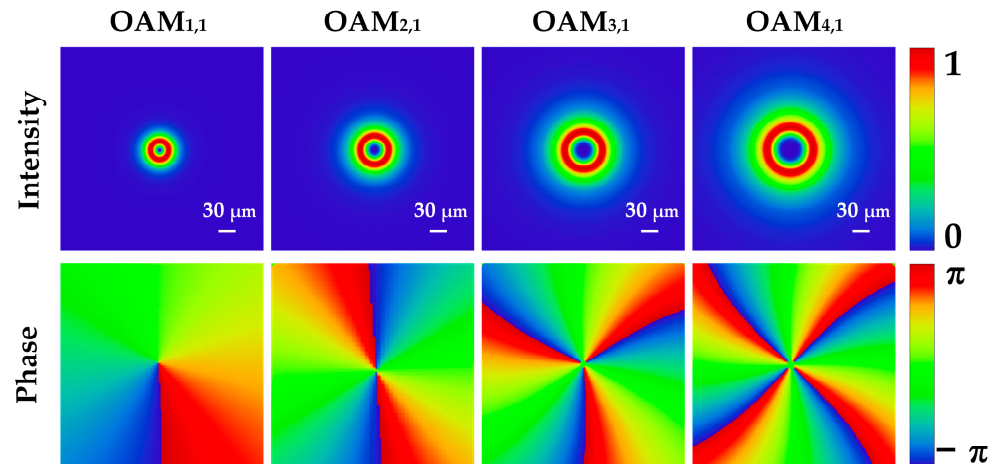


**Figure 2.** The normalized field intensity and phase distribution of OAM modes.

### 3. Fabrication

PbSe-doped RCF was prepared using MCVD technology by the following process [32]: Firstly, a quartz-based tube was heated to over 1700 °C with a hydrogen–oxygen flame to introduce  $\text{SiCl}_4$ ,  $\text{GeCl}_4$ , and borides. Secondly, a boride-doped inner-cladding layer was deposited. Thirdly, PbSe powder was deposited on the inner surface of the inner cladding via high-temperature evaporation. Subsequently, boride was introduced again to form a solid core. Finally, the preform was drawn into a PbSe-doped RCF with a specified geometric diameter. A cross-sectional image of the actual fiber and its refractive index distribution is presented in Figure 3a. The ring-core thickness was 8  $\mu\text{m}$ , and the refractive

index difference between the ring core and the inner cladding was 2.2%. Additionally, the fiber loss at 1550 nm was measured to be 0.25 dB/m using the truncation approach. The fluorescence spectrum of an optical fiber reveals its luminescent qualities. The fluorescence characteristics of the PbSe-doped RCF were measured using reverse pumping with a 980 nm laser, as shown in Figure 3b. The fluorescence ranged from 1150 nm to 1700 nm thanks to the different size distributions of PbSe QDs. The intensity of the fluorescence increased with increasing pumping power. At 800 mW, the fluorescence intensity ceased to increase and approached saturation, this is due to the complete inversion of particles in the PbSe QDs two-level system.

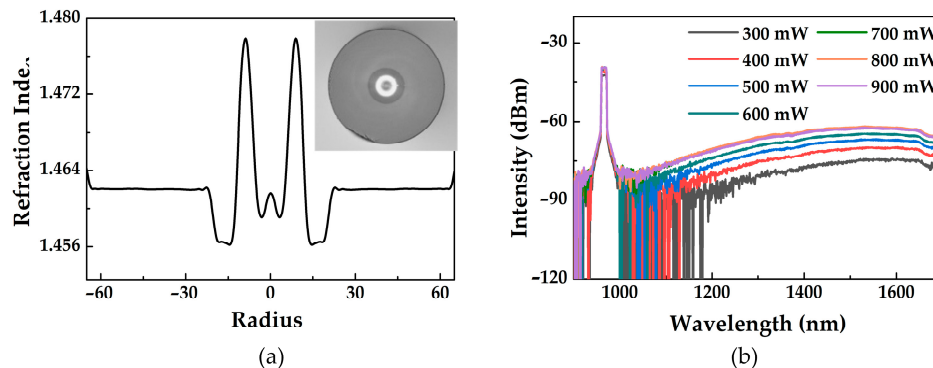


**Figure 3.** (a) Cross-section and refractive index profile curve of the PbSe-doped RCF; (b) Fluorescence spectrum of the fiber.

In this study, micro-SPP was fabricated using a two-photon professional 3D printing system (Nanoscribe). This technique enabled a resolution of 100 nm. The procedure was as follows: first, the end face of the PbSe-doped RCF was cleaned with acetone, isopropyl alcohol, and distilled water. After that, the photoresist (IP-Dip, Nanoscribe) was dropped into a  $63\times$  immersion objective, which focused the beam and wrote the structure directly on the end face of the fiber [33,34]. The two-photon photopolymerization effect was generated when the intensity of the focused beam exceeded the threshold intensity of the polymer. Finally, the samples were washed with propylene glycol monomethyl ether acetate and isopropyl alcohol. It took only a few minutes to print one SPP. The refractive index of the photoresist and that of the surrounding medium were 1.52 and 1. The incident wavelength suitable for the SPP was 1550 nm. The diameter and overall height of the SPP were 60  $\mu\text{m}$  and 5.98  $\mu\text{m}$ . SPPs with  $|l|=1, 2, 3, 4$  were printed sequentially. The SPP morphology at the center of the fiber was observed using an optical microscope, and the results are depicted in Figure 4.

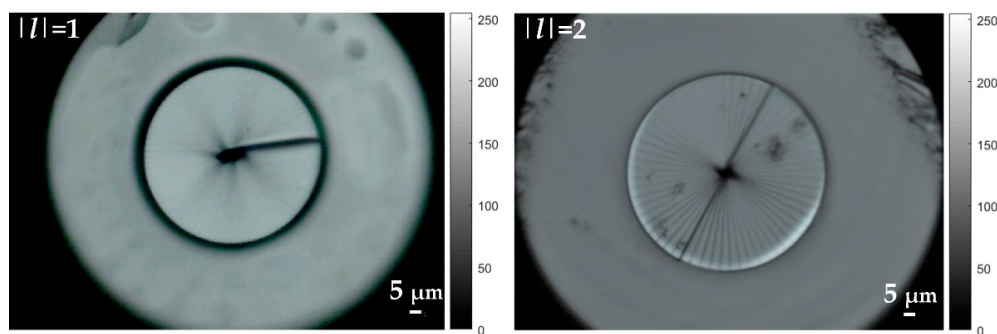


**Figure 4.** Images of SPP printed on the fiber end face.

#### 4. Experiments

##### 4.1. Generation and Transmission of OAM Modes

The OAM mode generation, transmission, and amplification systems constructed utilizing PbSe-doped RCF are depicted in Figure 5. A  $1 \times 2$  coupler divided the Gaussian

beam emitted by the 1550 nm laser into two beams. One beam was utilized as the transmitted signal beam, whereas the other beam was used as the reference beam for spherical interference. Before collimating the signal beam, a polarization controller (PC) was used to adjust the polarization direction. The dichroic mirror (DM) combined a signal beam with a 980 nm pump beam in free space. Subsequently, the combined beam was coupled to the SPP on the fiber end-face through a 20 $\times$  objective lens. The generated OAM beam by the SPP was transmitted through the PbSe-doped RCF for 20 m. The DM at the output of the fiber was used to filter out the residual pump beam.

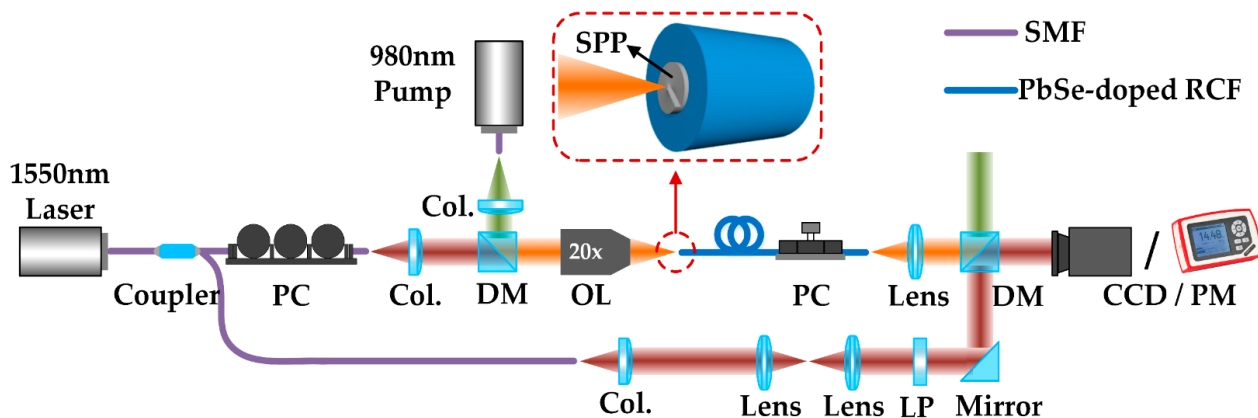


**Figure 5.** Schematic of the experimental setup for the OAM amplifier. PC: polarization controller; Col.: collimator; SMF: single-mode fiber; PbSe-doped RCF: PbSe-doped ring-core fiber; DM: dichroic mirror; OL: objective lens; SPP: spiral phase plate; LP: linear polarizer; PM: power meter.

The intensity distributions of the OAM modes ( $|l|=1, 2, 3, 4$ ) measured by the CCD are shown in Figure 6, along with the spiral interference fringes.

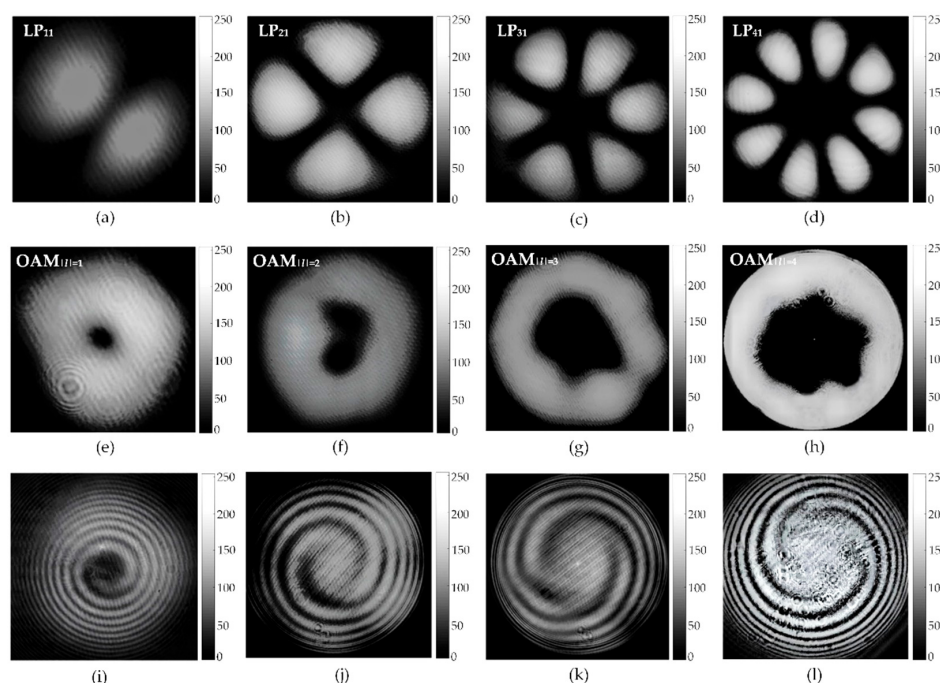


**Figure 6.** Spiral interferogram and intensity distribution of the OAM mode at 1550 nm: (a) Intensity of LP<sub>11</sub>; (b) Intensity of LP<sub>21</sub>; (c) Intensity of LP<sub>31</sub>; (d) Intensity of LP<sub>41</sub>; (e) Intensity of OAM<sub>|l|=1</sub>; (f) Intensity of OAM<sub>|l|=2</sub>; (g) Intensity of OAM<sub>|l|=3</sub>; (h) Intensity of OAM<sub>|l|=4</sub>; (i) Interference pattern of OAM<sub>|l|=1</sub>; (j) Interference pattern of OAM<sub>|l|=2</sub>; (k) Interference pattern of OAM<sub>|l|=3</sub>; (l) Interference pattern of OAM<sub>|l|=4</sub>.

The intensity of LP<sub>11</sub>, LP<sub>21</sub>, LP<sub>31</sub>, and LP<sub>41</sub> modes are shown in Figure 6a–d. Since the effective refractive index difference between the vector modes of the PbSe-doped RCF is less than  $1 \times 10^{-4}$ , the modes have degenerated to LP mode. The intensity of OAM<sub>||| = 1</sub>, OAM<sub>||| = 2</sub>, OAM<sub>||| = 3</sub>, and OAM<sub>||| = 4</sub> modes shown in Figure 6e–h can be observed by adjusting the PC to produce a phase difference of  $\pi/2$  between the odd and even modes of the LP mode. The interference fringes of each OAM mode are shown in Figure 6i–l. Here, we can see different spiral interference fringes [7], which indicates that we have successfully prepared SPPs with different topological charges. It is also demonstrated that the PbSe-doped RCF supports the transmission of OAM beams generated by SPPs.

#### 4.2. Amplification of OAM Modes

To evaluate the mode gain, an optical power meter was used to measure the total power before and after OAM mode amplification. The variation of on-off gain and DMG with pump power was investigated, as shown in Figure 7. The pump power varied from 42 mW to 634 mW and the experimental signal power and wavelength were  $-45$  dBm and 1550 nm, respectively. The maximum on-off gains for the OAM<sub>||| = 1</sub>, OAM<sub>||| = 2</sub>, OAM<sub>||| = 3</sub>, and OAM<sub>||| = 4</sub> modes were 14.9 dB, 13.9 dB, 13.2 dB, and 14 dB, respectively, while DMG was less than 1.7 dB. Evidently, the on-off gain increases with increasing pump power and tends to saturate. It primarily results from the fact that the particle number reversal in the PbSe QD energy level system gradually reaches saturation. The DMG values are generally small, which may be attributed to the pumping mode and the distribution of the PbSe QDs. The noise in fiber amplifiers is mostly caused by amplified spontaneous emission (ASE). Because the PbSe-doped RCF has a lower PbSe QD doping concentration, the ASE of the amplifier has less impact on the signal light.

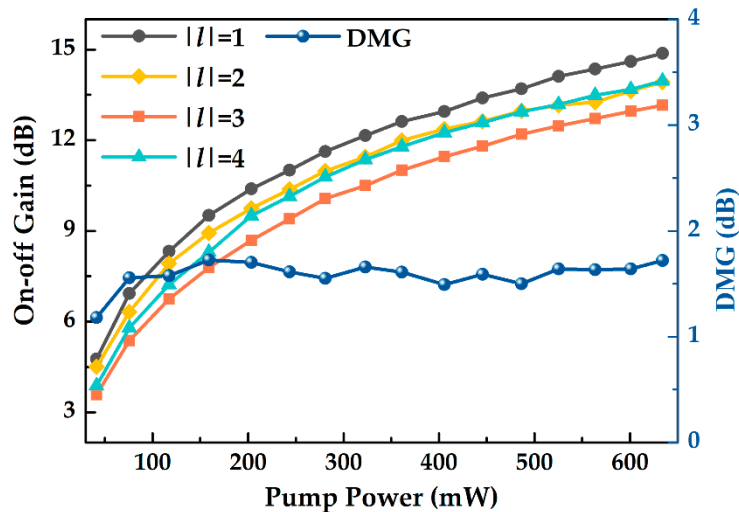
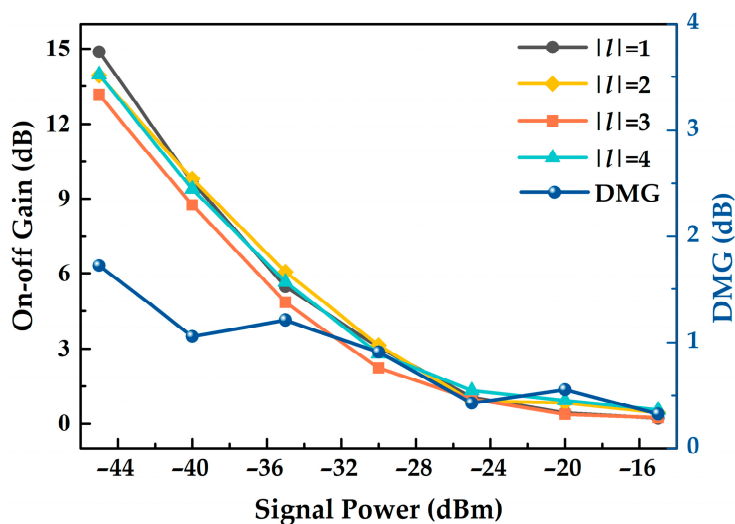


Figure 7. The OAM mode on-off gain and DMG versus pump power.

The relationship between the gain of each mode and the signal power is illustrated in Figure 8. When the pump output was 634 mW and the signal power changed between  $-45$  dBm and  $-15$  dBm, the on-off gain and the DMG both decreased as the input signal power increases. The gain was close to zero when the signal power was  $-15$  dBm or greater. This result may be explained by the fact that the number of particles at the upper energy level is continually depleted by the signal light but not efficiently refilled by the pump light. Therefore, the gain gradually decreases and approaches zero. During fiber preparation, PbSe is susceptible to vaporization under high-temperature heating, leading to a decreased concentration of PbSe doping, which, in turn, lowers the gain of the OAM mode.



**Figure 8.** The OAM mode on-off gain and DMG versus signal power.

In OAM-mode communication systems, the pump mode can affect the signal-mode gain and DMG, thereby compromising the balanced transmission of signals. The output mode of the 980 nm laser is the fundamental mode, but it turns into the OAM mode of the non-integral topological charge after passing the SPP with a wavelength of 1550 nm. According to Equation (2), when it passes through an SPP of 1550 nm with  $|l| = 1$ , it can produce an OAM beam with  $|l| = 1.58$ . The other orders are listed in Table 2.

**Table 2.** SPP orders at different wavelengths.

$l(\lambda = 1550 \text{ nm})$	$l(\lambda = 980 \text{ nm})$
1	1.58
2	3.16
3	4.74
4	6.33

## 5. Conclusions

In summary, we proposed and experimentally validated an amplifier system that integrates the generation, transmission, and amplification of the OAM beams. The PbSe-doped RCF was prepared using the MCVD method, and the microscale SPP was printed on its end face using 3D printing technology. This fiber supports the transmission of the OAM modes with  $|l| = 1, 2, 3, 4$ . At 1550 nm, the on-off gains are  $>13.2$  dB of four modes and DMG is  $<1.7$  dB. The following two aspects of the experiment can be optimized to improve the optical amplification gain: Firstly, optimizing the fiber preparation process, for example, by combining atomic layer deposition with MCVD technology to boost the doping of PbSe material. Secondly, the luminescence intensity of the fiber can be increased by using co-doping of active materials, thus improving the performance of the amplification system. In the future, the broadband amplification of higher-order OAM beams is expected to be achieved by preparing SPPs with different wavelengths and topological charges. Additionally, a micro-structured SPP is suitable for all-fiber OAM mode studies, owing to its structural stability, compactness, and integrability.

**Author Contributions:** H.W. (Huimei Wei), Y.S., H.W. (Heming Wei) and T.W. proposed the idea and conceptualization; H.W. (Huimei Wei) conducted the simulations; H.W. (Huimei Wei), H.W. (Heming Wei), K.W., Y.D. and Z.C. performed the experiment; Y.S., H.G., N.C. and F.P. performed scientific discussions and supervised the work; H.W. (Huimei Wei), Y.S. and H.G. helped with revision and organization of the paper; Y.S. and T.W. supported funding acquisition. All authors have read and agreed to the published version of the manuscript.

**Funding:** This research was funded by the National Natural Science Foundation of China (Grant No. 61875118, Grant No. 61675125, and Grant No. 61635006), and supported by 111 Project (Grant D20031).

**Institutional Review Board Statement:** Not applicable.

**Informed Consent Statement:** Not applicable.

**Data Availability Statement:** The data presented in this study are available on request from the corresponding author.

**Conflicts of Interest:** The authors declare no conflict of interest.

## References

1. Willner, A.E.; Huang, H.; Yan, Y.; Ren, Y.; Ahmed, N.; Xie, G.; Bao, C.; Li, L.; Cao, Y.; Zhao, Z.; et al. Optical communications using orbital angular momentum beams. *Adv. Opt. Photonics* **2015**, *7*, 66–106. [[CrossRef](#)]
2. Cheng, W.; Zhang, W.; Jing, H.; Gao, S.; Zhang, H. Orbital angular momentum for wireless communications. *IEEE Wirel. Commun.* **2018**, *26*, 100–107. [[CrossRef](#)]
3. Pang, F.; Xiang, L.; Liu, H.; Zhang, L.; Wen, J.; Zeng, X.; Wang, T. Review on fiber-optic vortices and their sensing applications. *J. Lightwave Technol.* **2021**, *39*, 3740–3750. [[CrossRef](#)]
4. Geday, M.A.; Caño-García, M.; Otón, J.M.; Quintana, X. Adaptive spiral diffractive lenses—Lenses with a twist. *Adv. Opt. Mater.* **2020**, *8*, 2001199. [[CrossRef](#)]
5. Zhang, Y.; Wang, J.; Qian, X.; Zhu, W.; Li, J. Orbital angular momentum evolution of twisted multi-Gaussian Schell model beams in anisotropic turbulence. *Opt. Commun.* **2022**, *520*, 128454. [[CrossRef](#)]
6. Jung, Y.; Alam, S.U.; Richardson, D.J.; Ramachandran, S.; Abedin, K.S. Multicore and multimode optical amplifiers for space division multiplexing. In *Optical Fiber Telecommunications VII*; Willner, A.E., Ed.; Academic Press: New York, NY, USA, 2020; pp. 301–333. [[CrossRef](#)]
7. Bai, Y.; Lv, H.; Fu, X.; Yang, Y. Vortex beam: Generation and detection of orbital angular momentum. *Chin. Opt. Lett.* **2022**, *20*, 012601. [[CrossRef](#)]
8. Yang, D.; Lin, J.; Chen, C.; Li, C.; Hao, J.; Lv, B.; Zhou, K.; Wang, Y.; Jin, P. Multiwavelength high-order optical vortex detection and demultiplexing coding using a metasurface. *Adv. Photonics Nexus* **2022**, *1*, 016005. [[CrossRef](#)]
9. Krenn, M.; Handsteiner, J.; Fink, M.; Fickler, R.; Ursin, R.; Malik, M.; Zeilinger, A. Twisted light transmission over 143 km. *Proc. Natl. Acad. Sci. USA* **2016**, *113*, 13648–13653. [[CrossRef](#)]
10. Zhang, X.; Liu, J.; Chen, S.; Li, W.; Du, C.; Wang, J. Amplification of 14 orbital angular momentum modes in ring-core erbium-doped fiber with high modal gain. *Opt. Lett.* **2021**, *46*, 5647–5650. [[CrossRef](#)]
11. Mehta, A.; Rehan, M.; Rastogi, V. Erbium-doped circular photonic crystal fiber design for the amplification of 20 OAM modes. *J. Opt. Soc. Am. B* **2021**, *38*, F138–F144. [[CrossRef](#)]
12. Wen, T.; Gao, S.; Li, W.; Tu, J.; Du, C.; Zhou, J.; Ao, Z.; Zhang, B.; Liu, W.; Li, Z. Third-and fourth-order orbital angular momentum multiplexed amplification with ultra-low differential mode gain. *Opt. Lett.* **2021**, *46*, 5473–5476. [[CrossRef](#)] [[PubMed](#)]
13. Liu, S.; Zhang, L.; Jiang, Q.; Xue, X.; Wen, J.; Chen, W.; Pang, F.; Wang, T. The Performance of Orbital Angular Momentum Mode ( $|l| = 1\sim 3$ ) Amplification Based on Ring-Core Erbium-Doped Fibers. *Photonics* **2022**, *9*, 491. [[CrossRef](#)]
14. Caño-García, M.; Quintana, X.; Otón, J.M.; Geda, M.A. Dynamic multilevel spiral phase plate generator. *Sci. Rep.* **2018**, *8*, 15804. [[CrossRef](#)] [[PubMed](#)]
15. Yan, L.; Gregg, P.; Karimi, E.; Rubano, A.; Marrucci, L.; Boyd, R.; Ramachandran, S. Q-plate enabled spectrally diverse orbital-angular-momentum conversion for stimulated emission depletion microscopy. *Optica* **2015**, *2*, 900–903. [[CrossRef](#)]
16. Zhou, J.; Lin, P.T. Generation of mid-infrared vortex beams by 3-D printed polymer phase plates. *Opt. Laser Technol.* **2022**, *156*, 108509. [[CrossRef](#)]
17. Wu, G.B.; Chan, K.F.; Chan, C.H. 3-D printed terahertz lens to generate higher order Bessel beams carrying OAM. *IEEE Trans. Antennas Propag.* **2021**, *69*, 3399–3408. [[CrossRef](#)]
18. Lightman, S.; Gvishi, R.; Hurvitz, G.; Arie, A. Shaping of light beams by 3D direct laser writing on facets of nonlinear crystals. *Opt. Lett.* **2015**, *40*, 4460–4463. [[CrossRef](#)]
19. Liu, C.; Hu, C.; Wei, D.; Chen, M.; Shi, J.; Wang, H.; Xie, C.; Zhang, X. Generating convergent Laguerre-Gaussian beams based on an arrayed convex spiral phaser fabricated by 3D printing. *Micromachines* **2020**, *11*, 771. [[CrossRef](#)]
20. Stegenburgs, E.; Bertoncini, A.; Trichili, A.; Alias, M.S.; Ng, T.K.; Alouini, M.S.; Ooi, B.S. Near-infrared OAM communication using 3D-printed microscale spiral phase plates. *IEEE Commun. Mag.* **2019**, *57*, 65–69. [[CrossRef](#)]
21. Yu, J.; Bai, Z.; Zhu, G.; Fu, C.; Li, Y.; Liu, S.; Liao, C.; Wang, Y. 3D nanoprinted kinoform spiral zone plates on fiber facets for high-efficiency focused vortex beam generation. *Opt. Exp.* **2020**, *28*, 38127–38139. [[CrossRef](#)]
22. Weber, K.; Hütt, F.; Thiele, S.; Gissibl, T.; Herkommer, A.; Giessen, H. Single mode fiber based delivery of OAM light by 3D direct laser writing. *Opt. Exp.* **2017**, *25*, 19672–19679. [[CrossRef](#)] [[PubMed](#)]
23. Wei, H.; Amritanath, A.K.; Krishnaswamy, S. 3D printing of micro-optic spiral phase plates for the generation of optical vortex beams. *IEEE Photonics Technol. Lett.* **2019**, *31*, 599–602. [[CrossRef](#)]

24. Jung, Y.; Kang, Q.; Sidharthan, R.; Ho, D.; Yoo, S.; Gregg, P.; Ramachandran, S.; Alam, S.; Richardson, D.J. Optical orbital angular momentum amplifier based on an air-hole erbium-doped fiber. *J. Lightwave Technol.* **2017**, *35*, 430–436. [[CrossRef](#)]
25. Liu, J.; Chen, S.; Wang, H.; Zheng, S.; Zhu, L.; Wang, A.; Wang, J. Amplifying orbital angular momentum modes in ring-core erbium-doped fiber. *Research* **2020**, *2020*, 7623751. [[CrossRef](#)]
26. Ma, J.; Xia, F.; Chen, S.; Li, S.; Wang, J. Amplification of 18 OAM modes in a ring-core erbium-doped fiber with low differential modal gain. *Opt. Exp.* **2019**, *27*, 38087–38097. [[CrossRef](#)]
27. Watekar, P.R.; Ju, S.; Lin, A.; Kim, M.J.; Lee, B.H.; Han, W.T. Linear and nonlinear optical properties of the PbSe quantum dots doped germano-silica glass optical fiber. *J. Non-Cryst. Solids.* **2021**, *356*, 2384–2388. [[CrossRef](#)]
28. Zhang, L.; Huang, T.; Ning, L.; Li, S.; Zheng, Y. Effects of doped material properties on the emission of quantum dot optical fiber. *Opt. Fiber Technol.* **2020**, *58*, 102305. [[CrossRef](#)]
29. Cheng, C.; Hu, N.; Cheng, X. Experimental realization of a PbSe quantum dot doped fiber amplifier with ultra-bandwidth characteristic. *Opt. Commun.* **2017**, *382*, 470–476. [[CrossRef](#)]
30. Shen, Y.; Ren, G.; Yang, Y.; Yao, S.; Xiao, S.; Jiang, Y.; Xu, Y.; Wu, Y.; Jin, W.; Jian, S. Generation of the tunable second-order optical vortex beams in narrow linewidth fiber laser. *IEEE Photonics Technol. Lett.* **2017**, *29*, 1659–1662. [[CrossRef](#)]
31. Meng, M.; Yan, D.; Cao, M.; Li, X.; Qiu, G.; Li, J. Design of negative curvature fiber carrying multiorbital angular momentum modes for terahertz wave transmission. *Results Phys.* **2021**, *29*, 104766. [[CrossRef](#)]
32. Xu, L.; Shang, Y.; Yang, J.; Chen, Z.; Pang, F.; Liu, H.; Dong, Y.; Chen, N.; Wen, J.; Wang, T. Orbital Angular Momentum Optical Amplifier Based on PbS-Doped Ring-Core Fiber. *Front. Phys.* **2020**, *8*, 198. [[CrossRef](#)]
33. Zhang, D.; Wei, H.; Hu, H.; Krishnaswamy, S. Highly sensitive magnetic field microsensor based on direct laser writing of fiber-tip optofluidic Fabry-Perot cavity. *APL Photon.* **2020**, *5*, 076112. [[CrossRef](#)]
34. Hadibrata, W.; Wei, H.; Krishnaswamy, S.; Aydin, K. Inverse design and 3D printing of a metalens on an optical fiber tip for direct laser lithography. *Nano Lett.* **2021**, *21*, 2422–2428. [[CrossRef](#)] [[PubMed](#)]